Applied Thermal Engineering 109 (2016) 22–34

Contents lists available at ScienceDirect

Applied Thermal Engineering

journal homepage: www.elsevier.com/locate/apthermeng

Research Paper

Thermal design exploration of a swirl flow microchannel heat sink for high heat flux applications based on numerical simulations

Benjamín Herrmann-Priesnitz [a,*], Williams R. Calderón-Muñoz [a,b], Alvaro Valencia [a], Rodrigo Soto [c]

[a] Department of Mechanical Engineering, Universidad de Chile, Beauchef 851, Santiago, Chile
[b] Energy Center, Universidad de Chile, Av. Tupper 2007, Santiago, Chile
[c] Physics Department, Universidad de Chile, Av. Blanco Encalada 2008, Santiago, Chile

HIGHLIGHTS

- Numerical simulations of flow in a swirl microchannel heat sink are presented.
- Pressure drop and heat flux were analyzed for different designs.
- Rotation of the fluid induces crossflow which modifies boundary layer structure.
- Performance is enhanced using a small flow inlet angle and changing to a nanofluid.
- Due to the crossflow, heat flux may not increase with a decrease in channel height.

ARTICLE INFO

Article history:
Received 7 June 2016
Revised 6 August 2016
Accepted 9 August 2016
Available online 9 August 2016

Keywords:
Laminar flow
Boundary layer
Convective heat transfer
Nanofluid
Swirl flow heat sink

ABSTRACT

Numerical simulations of velocity and temperature fields to explore the design of a single phase microchannel cooling system with spiraling radial inflow for high heat flux applications are presented. Total pressure drop and average wall heat flux are calculated for different flow rates and the effects of changing the microchannel height, flow inlet angle, and working fluid are investigated. Rotation of the fluid induces a crossflow and entrainment, this is found to enhance convective heat transfer considerably due to motion of fluid towards the heat exchange surface. The strength of this effect depends on the structure of hydrodynamic boundary layers, which is characterized by the Reynolds number and the flow inlet angle. The effect of reducing the Prandtl number is evaluated changing the working fluid from water to a 2 vol% and a 4 vol% water-Cu nanofluid suspension. For the cases studied, it is found that heat transfer enhancement by increasing the inlet swirl is greater than that of decreasing the Prandtl number using a nanofluid, though at a much higher pumping cost. In order to improve the performance of the device for high heat flux applications, admission of the flow should be as tangential as practically possible. It is found that, when reducing the microchannel height, boundary layers may merge and the entrainment effect is lost, therefore the total heat flux may not always increase with a decrease of the flow passage area, as opposed to conventional microchannels. The swirl flow microchannel heat sink showed promising cooling characteristics for applications such as thermal management of electronics or concentrated photovoltaics, with a ratio of pumping cost to heat rate of 0.02% for the base design studied.

1. Introduction

High heat flux removal is required in numerous industrial applications, such as electronics cooling [1], laser diodes cooling [2], and concentrated photovoltaics [3]. Thermal management is important for the performance, safety, and lifetime of these devices [4,5], which is why high heat flux cooling technologies is one of the most active fields of heat transfer research today. Most promising solutions using single phase liquid cooled heat sinks include designs with jet impingement, flow through porous media, and microchannels [6–8].

A novel swirl flow microchannel heat sink was designed and studied by Ruiz and Carey [9,10]. The authors built a prototype and compared experimental measurements using water to an analytical model for the heat and momentum transport in the heat sink. They found that the model underpredicted both, the pressure drop and total heat flux, due to not taking into account secondary

* Corresponding author.
E-mail address: bherrman@ing.uchile.cl (B. Herrmann-Priesnitz).

http://dx.doi.org/10.1016/j.applthermaleng.2016.08.054
1359-4311/

Nomenclature

C_p	heat capacity
C_u	cell Courant number
$\mathcal{D}_c$	Chebyshev differentiation matrix
$f(\eta)$	streamwise velocity profile
$g(\eta)$	crossflow velocity profile
h	microchannel height
$\dot{m}$	mass flow rate
n	particle shape factor
N_z	grid points in the z direction
Nu	average Nusselt number
p	pressure
Pr	Prandtl number
q	velocity magnitude
q''_w	average wall heat flux
Q_p/Q_t	ratio of pumping power to heat rate
r	radial coordinate
R_{hs}	thermal resistance
Re	reduced Reynolds number
Re_δ	Bödewadt Reynolds number
Re_o	flow rate Reynolds number
T	temperature
T_m	mean temperature
u	radial velocity
U_o	dimensionless radial inlet velocity
v	tangential velocity
$\dot{V}$	volumetric flow rate
$\dot{V}_{max}$	maximum volumetric flow rate
V_o	dimensionless tangential inlet velocity
w	axial velocity
x	transformed radial coordinate
z	axial coordinate

Greek symbols

α	thermal diffusivity
α_0–α_5	integral method constants
β	flow inlet angle
β_e	thermal expansion coefficient
Δp	total pressure loss
Δt	time step
Δx	step size in the x direction
Δz	step size in the z direction
δ	boundary layer thickness
ϵ	cavity aspect ratio
η	boundary layer coordinate
γ	ratio of tangential to radial inlet velocity
λ	thermal conductivity
μ	dynamic viscosity
ν	kinematic viscosity
ϕ	particle volume fraction
ρ	density
Θ	dimensionless temperature
θ	azimuthal coordinate
ε	ratio of streamwise to crossflow velocity

Superscripts & subscripts

$*$	dimensional variable
c	variable at the inviscid core
eff	property of the nanofluid
f	property of base fluid
i	variable at the inner radius
j	position in the x direction
k	position in the z direction
n	crossflow component
o	variable at the outer radius
p	property of the solid particle
s	streamwise component
w	variable at the lower wall

flows induced by rotation. Ruiz and Carey results also showed that the design is promising, a heat flux of 113 W/cm^2 was achieved while maintaining a surface temperature below 80 °C and a ratio of pumping power to heat rate of 0.03% [9,10]. The swirl flow microchannel heat sink consists on a cylindrical cavity where fluid is admitted through the periphery, spirals radially inward and exits through the center, heat is removed from one of the cavity walls whereas the other is insulated. The device is classified as a microchannel when the height of the cavity is in the range of 50–1000 μm. A schematic of the heat sink design is shown in Fig. 1.

Rotating flow inside a cylindrical cavity is of basic interest in fluid mechanics. Throughout several decades, the problem has been addressed by many authors with different approaches and for different applications. Parallel disk turbomachinery was studied extensively by W. Rice, who did experimental measurements along with theoretical and numerical calculations [11–13]. In 1969, Wormley formulated an analytical model for short vortex chambers, and calculated the development of entraining and non entraining boundary layers in a non rotating cavity with radial inflow [14]. Owen et al. studied the case of radial inflow in a rotating cavity, solved non entraining boundary layers with integral methods and entraining boundary layers with a simple free disk or free vortex model. The line of work of these authors has continued the research of this flow with applications in cooling systems for gas turbines [15–18]. Herrmann-Priesnitz et al. studied the development of boundary layers in rotating cylindrical cavities with steady radial inflow [19]. In particular, an integral method was used to solve mass and momentum transfer coupled between boundary layers and an inviscid core region. Most research on heat transfer in cylindrical cavities has involved radial outflow in rotating and non-rotating configurations. Mochizuki and Yang conducted experimental studies of the heat transfer and friction loss for radial outflow and observed three distinct flow regimes: steady laminar, periodic laminar, and turbulent [20,21]. Similar experiments were conducted by Suryanarayana et al. [22] who found correlations for the average Nusselt number and studied the effect of rotation. Devienne and Cognet studied experimentally the case of spiraling radial inflow for Newtonian and non-Newtonian fluids, and found the existence of secondary flows which are important for heat transfer [23].

Conventional process fluids, such as oil, water, and ethylene glycol mixture are poor heat transfer fluids because of their low thermal conductivity. Over the last decade, convective heat transfer enhancement with nanofluids has been an active research topic [24–29]. Nanofluids are colloidal suspensions with solid particle diameters of 1–100 nm, and are considered to offer important advantages over conventional heat transfer fluids. The materials of suspended nanoparticles, such as Al_2O_3, CuO, Cu, SiO, and TiO, have a thermal conductivity which is much higher than the base fluid. Therefore, the effective thermal conductivity of the suspension is significantly higher than that of the base fluid, thus increasing heat transfer substantially even at low concentrations [27]. Heat transfer using Al_2O_3 nanofluids in a cylindrical cavity with radial outflow was studied numerically by Roy et al. and also

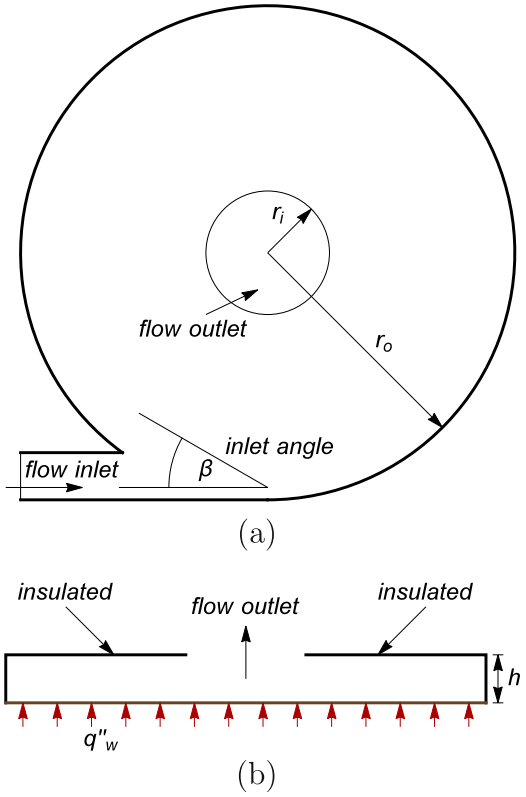

Fig. 1. Schematic of the design of a swirl flow microchannel heat sink: (a) Top view. (b) Cross-sectional view.

experimentally by Gherasim et al., heat transfer enhancement at an additional pumping cost was observed [30–32].

The same method presented in Ref. [19] is used in this article to solve the velocity field in a non rotating cavity which models the swirl flow microchannel heat sink. First, the structure of hydrodynamic boundary layers is investigated and the influence of a Reynolds number and the flow inlet angle over the flow patterns is analyzed. Then, the temperature distribution is calculated by solving the energy equation using a time marching technique. Rotation of the fluid induces a crossflow and entrainment, this is found to enhance convective heat transfer considerably due to motion of fluid towards the heat exchange surface. This effect depends on the structure of hydrodynamic boundary layers, and is intensified for small flow inlet angles and high Reynolds.

The effects of varying the cavity height, the flow inlet angle, and the Prandtl number on the heat sink performance are investigated. When reducing the microchannel height, boundary layers may merge and the entrainment effect is lost, therefore the total heat flux may not always increase with a decrease of the flow passage area, as opposed to conventional microchannels. It is found that, for high heat flux applications, admission of the flow should be as tangential as practically possible. For the Prandtl number variation, heat sink performance using water is compared to that of using a 2 vol% and a 4 vol% water-Cu nanofluid. We compare the benefits of changing to a nanofluid to the performance increase obtained with geometric design variations. For the cases studied, it is found that heat transfer enhancement by increasing the inlet swirl is greater than that obtained when reducing the Prandtl number using a nanofluid, though at a much higher pumping cost. The swirl flow microchannel heat sink showed promising cooling characteristics for high heat flux applications, with a ratio of pumping cost to heat rate of 0.02% for the base design studied. Finally, we comment on the physical considerations, review the validity of the assumptions made, and consider future lines of work.

2. Governing equations

In this section, the governing equations for the flow in cylindrical cavity with imposed radial inflow are presented. The cavity has a height h, an outer radius r_o where the flow enters, and an inner radius r_i where the flow exits. Using the cylindrical system of coordinates shown in Fig. 2, the velocity components are denoted $u\hat{r} + v\hat{\theta} + w\hat{z}$.

Mass, momentum, and energy balances for the working fluid are governed by continuity, Navier-Stokes and thermal energy equations respectively. The main assumptions are that the fluid is incompressible, with constant physical properties, that the flow is in steady-state and has axisymmetry, and that buoyant effects as well as viscous dissipation are neglected. With these assumptions, the governing equations become:

$$\frac{\partial u^*}{\partial r^*} + \frac{u^*}{r^*} + \frac{\partial w^*}{\partial z^*} = 0, \tag{1}$$

$$u^*\frac{\partial u^*}{\partial r^*} + w^*\frac{\partial u^*}{\partial z^*} - \frac{v^{*2}}{r^*} = -\frac{1}{\rho}\frac{\partial p^*}{\partial r^*} + \nu\left(\frac{\partial^2 u^*}{\partial z^{*2}} + \frac{\partial}{\partial r^*}\left(\frac{u^*}{r^*}\right) + \frac{\partial^2 u^*}{\partial r^{*2}}\right), \tag{2}$$

$$u^*\frac{\partial v^*}{\partial r^*} + w^*\frac{\partial v^*}{\partial z^*} + \frac{u^* v^*}{r^*} = \nu\left(\frac{\partial^2 v^*}{\partial z^{*2}} + \frac{\partial}{\partial r^*}\left(\frac{v^*}{r^*}\right) + \frac{\partial^2 v^*}{\partial r^{*2}}\right), \tag{3}$$

$$u^*\frac{\partial w^*}{\partial r^*} + w^*\frac{\partial w^*}{\partial z^*} = -\frac{1}{\rho}\frac{\partial p^*}{\partial z^*} + \nu\left(\frac{\partial^2 w^*}{\partial z^{*2}} + \frac{1}{r^*}\frac{\partial w^*}{\partial r^*} + \frac{\partial^2 w^*}{\partial r^{*2}}\right), \tag{4}$$

$$u^*\frac{\partial T^*}{\partial r} + w^*\frac{\partial T^*}{\partial z^*} = \alpha\left(\frac{\partial^2 T^*}{\partial z^{*2}} + \frac{\partial}{\partial r^*}\left(\frac{T^*}{r^*}\right) + \frac{\partial^2 T^*}{\partial r^{*2}}\right), \tag{5}$$

where $(\,)^*$ denotes dimensional variables, p is the static pressure, and T is the temperature. The fluid has density ρ, kinematic viscosity ν, and thermal diffusivity α. Governing equations are nondimensionalized by scaling flow variables as follows:

$$r = \frac{r^*}{r_o}, \quad z = \frac{z^*}{h/2}, \quad u = \frac{u^*}{q_o}, \quad v = \frac{v^*}{q_o}, \quad p = \frac{p^*}{\rho\, q_o^2}, \quad \Theta = \frac{T - T_o}{T_w - T_o},$$

where $h/2$ is used as vertical length scale, r_o as horizontal length scale and the magnitude of the velocity at the inlet of the cavity,

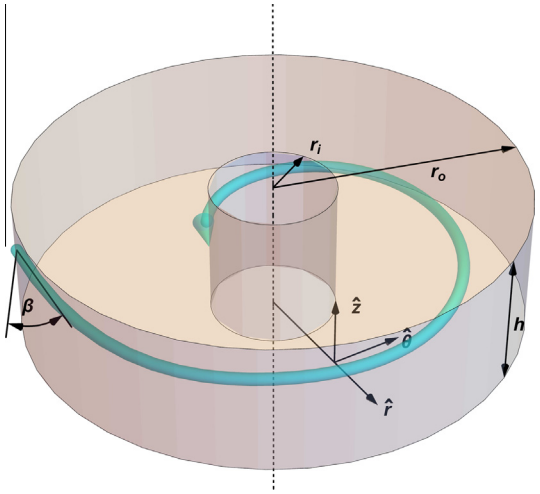

Fig. 2. Cavity with radial inflow and cylindrical system of coordinates.

$q_o = \sqrt{u_o^2 + v_o^2}$, is used as the scale for the velocities u and v. Pressure is nondimensionalized using the scale of the inertial terms, and T is scaled using the temperature at the inlet (outer radius), T_o, and the wall temperature T_w. From the continuity equation, Eq. (1), it follows that proper scaling for the axial velocity component is $w = \frac{w^*}{\epsilon\, q_o}$. Where $\epsilon = \frac{h/2}{r_o}$ is the aspect ratio of the cavity. Therefore, the nondimensional form of Eqs. (1)–(5) is:

$$\frac{\partial u}{\partial r} + \frac{u}{r} + \frac{\partial w}{\partial z} = 0, \tag{6}$$

$$u\frac{\partial u}{\partial r} + w\frac{\partial u}{\partial z} - \frac{v^2}{r} = -\frac{\partial p}{\partial r} + \frac{1}{Re}\left[\frac{\partial^2 u}{\partial z^2} + \epsilon^2\left(\frac{\partial}{\partial r}\left(\frac{u}{r}\right) + \frac{\partial^2 u}{\partial r^2}\right)\right], \tag{7}$$

$$u\frac{\partial v}{\partial r} + w\frac{\partial v}{\partial z} + \frac{uv}{r} = \frac{1}{Re}\left[\frac{\partial^2 v}{\partial z^2} + \epsilon^2\left(\frac{\partial}{\partial r}\left(\frac{v}{r}\right) + \frac{\partial^2 v}{\partial r^2}\right)\right], \tag{8}$$

$$\epsilon^2\left(u\frac{\partial w}{\partial r} + w\frac{\partial w}{\partial z}\right) = -\frac{\partial p}{\partial z} + \frac{\epsilon^2}{Re}\left[\frac{\partial^2 w}{\partial z^2} + \epsilon^2\left(\frac{1}{r}\frac{\partial w}{\partial r} + \frac{\partial^2 w}{\partial r^2}\right)\right], \tag{9}$$

$$u\frac{\partial \Theta}{\partial r} + w\frac{\partial \Theta}{\partial z} = \frac{1}{RePr}\left[\frac{\partial^2 \Theta}{\partial z^2} + \epsilon^2\left(\frac{\partial}{\partial r}\left(\frac{\Theta}{r}\right) + \frac{\partial^2 \Theta}{\partial r^2}\right)\right], \tag{10}$$

these equations include a reduced Reynolds number, Re, and a Prandtl number, Pr. These nondimensional numbers are defined as follows:

$$Re = \epsilon\frac{q_o h/2}{\nu} = \frac{q_o\, h^2}{4\nu\, r_o}, \qquad Pr = \frac{\nu}{\alpha}.$$

For a cavity with small aspect ratio $\epsilon \ll 1$, the terms of order $\mathcal{O}\epsilon^2$ can be neglected in Eqs. (6)–(10). This results in the boundary layer approximation form of equations. The variable $x = 1 - r$ is exchanged with r, so that the cavity inlet becomes $x = 0$ and its center is $x = 1$. The radial velocity u is redefined as positive in the $+x$ direction (inward). Therefore, the nondimensional equations of motion with the boundary layer approximation are:

$$\frac{\partial u}{\partial x} - \frac{u}{(1-x)} + \frac{\partial w}{\partial z} = 0. \tag{11}$$

$$u\frac{\partial u}{\partial x} + w\frac{\partial u}{\partial z} + \frac{v^2}{(1-x)} = -\frac{\partial p}{\partial x} + \frac{1}{Re}\frac{\partial^2 u}{\partial z^2}, \tag{12}$$

$$u\frac{\partial v}{\partial x} + w\frac{\partial v}{\partial z} - \frac{uv}{(1-x)} = \frac{1}{Re}\frac{\partial^2 v}{\partial z^2}, \tag{13}$$

$$0 = -\frac{\partial p}{\partial z}, \tag{14}$$

$$u\frac{\partial \Theta}{\partial x} + w\frac{\partial \Theta}{\partial z} = \frac{1}{RePr}\frac{\partial^2 \Theta}{\partial z^2}. \tag{15}$$

Due to the boundary layer approximation, the original elliptic partial differential equation (PDE) problem reduces to Eqs. (11)–(15), which is a parabolic PDE problem. Boundary conditions selected to model the swirl flow microchannel heat sink are shown in Fig. 3.

In Fig. 3, U_o and V_o are the nondimensional velocities specified at the inlet and $x_i = 1 - r_i/r_o$. For temperature, the boundary condition at the upper wall is adiabatic and at the lower wall constant temperature T_w is specified, whereas a no slip boundary condition is used for the velocity at both walls. Constant temperature boundary condition is preferred because we are interested in the heat rate that can be obtained with a device designed to keep the wall

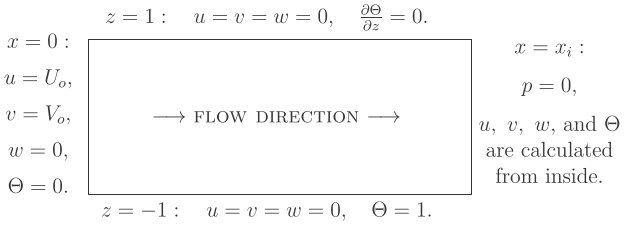

Fig. 3. Thermal problem boundary conditions.

temperature under $T_w = 80\,^{\circ}\mathrm{C}$, which is a requirement for applications such as thermal management of electronics [6,9]. The reference pressure is set at the outlet, $x = x_i$. The system of Eqs. (11)–(15) along with the boundary conditions shown in Fig. 3 conform a well-posed parabolic PDE problem. If the angle that the velocity vector at the inlet makes with the tangent of the cavity is $\beta = \arctan(U_o/V_o)$, then the nondimensional numbers that characterize the problem are β, Re and Pr.

3. Numerical methods

In Eqs. (11)–(14) the velocity field is uncoupled from the temperature field. In fact, using the boundary conditions shown in Fig. 3, a solution for u, v, w and p can be obtained independently and then used to solve the Eq. (15) for Θ. The numerical methods used to solve both, the velocity field and then the temperature field, are presented in the following sections.

3.1. Velocity field

An integral method to solve rotating boundary layer flows inside cylindrical cavities was developed by Herrmann-Priesnitz et al. [19]. First, the flow is modeled considering two regions, (i) wall boundary layers where viscous effects are important, and (ii) an inviscid core region. Eq. (14) states that the static pressure remains constant through height of the cavity in the z direction. Inside the boundary layers, flow velocities in the radial and tangential directions are functions of x and z, while at the core they are assumed to depend only on x and are denoted as u_c and v_c. Fig. 4 shows three possible radial velocity profiles that can be found for rotating flows inside a cylindrical cavity.

If the flow enters the cavity with a uniform velocity profile, very close to the inlet the radial velocity profile will resemble Fig. 4a. Due to rotational effects, a crossflow is induced inside the boundary layers, a maximum appears in the radial velocity and fluid from the core is drawn towards the walls. At the same time, boundary

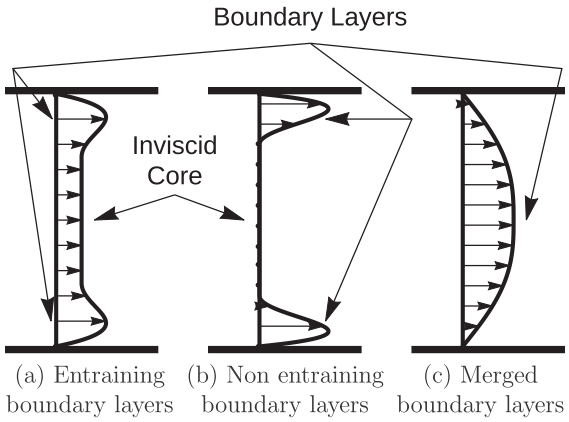

Fig. 4. Scheme of possible radial velocity profiles in a rotating cylindrical cavity.

Table 1
Sensitivity analysis of the first step size.

First step size	δ at position		
$\Delta x \times 10^8$	$x = 0$	$x = 1 \times 10^{-6}$	$x = 0.005$
0.5	0.0007	0.0116	0.5342
1	0.0010	0.0117	0.5342
5	0.0022	0.0118	0.5342

layers tend to grow. These two effects, flow entrainment and boundary layers thickening, compete against each other. Depending on the nondimensional numbers that characterize the hydrodynamics problem, β and Re, the boundary layers may develop into the scenarios shown in Fig. 4b or c. Radial velocity profile shown in Fig. 4b corresponds to a case where, due to strong rotational effects, radial velocity in the core region becomes $u_c = 0$, which is expected for high Re and low β. In this case, all the radial flow is forced to pass through the boundary layers and the fluid in the core remains in rotation without leaving the cavity. Radial velocity profile shown in Fig. 4c corresponds to a case where, due to strong viscous effects, boundary layers grow until they merge. In this case, the core region disappears and velocity profiles are nearly parabolic, which is expected for low values of Re. Therefore, the structure of the hydrodynamic boundary layers is classified by considering these three possible scenarios: entraining, non entraining, and merged boundary layers.

A system of equations is obtained by considering mass and momentum transport coupled between these two regions, boundary layers and inviscid core. The continuity equation, Eq. (11), is integrated across the cavity height, and momentum equations, Eqs. (12)–(14), are integrated inside the boundary layers.

Integral continuity:

$$\int_0^1 \frac{\partial u}{\partial x}\mathrm{d}z - \int_0^1 \frac{u}{(1-x)}\mathrm{d}z = 0. \tag{16}$$

Integral boundary layer x-momentum:

$$\int_0^\delta \left(\frac{\partial u^2}{\partial x} - u_c\frac{\partial u}{\partial x} + \frac{v^2 + u_c u - u^2}{(1-x)}\right)\mathrm{d}z = -\delta\,\frac{\mathrm{d}p}{\mathrm{d}x} - \frac{1}{Re}\frac{\partial u}{\partial z}\bigg|_{z=0}. \tag{17}$$

Integral boundary layer θ-momentum:

$$\int_0^\delta \left(\frac{\partial u v}{\partial x} - v_c\frac{\partial u}{\partial x} + \frac{u v_c - 2uv}{(1-x)}\right)\mathrm{d}z = -\frac{1}{Re}\frac{\partial v}{\partial z}\bigg|_{z=0}. \tag{18}$$

Core x−momentum:

$$u_c\frac{\mathrm{d}u_c}{\mathrm{d}x} + \frac{v_c^2}{(1-x)} = -\frac{\mathrm{d}p}{\mathrm{d}x}. \tag{19}$$

Core θ−momentum:

$$u_c\frac{\mathrm{d}v_c}{\mathrm{d}x} - \frac{u_c v_c}{(1-x)} = 0. \tag{20}$$

In Eqs. (16)–(20), δ is the thickness of the boundary layer, and the z coordinate is shifted so that $z = 0$ is at one of the cavity walls and $z = 1$ is at the cavity mid-plane. It is assumed that the shear stress vanishes at the inviscid core and the velocity components are matched to those at the edge of the boundary layer, that is $u = u_c$ and $v = v_c$ at $z = \delta$. Boundary conditions are:

$$\begin{aligned}
&\text{at } z = 0: \quad u = v = w = 0,\\
&\text{at } z = 1: \quad w = \frac{\partial u}{\partial z} = \frac{\partial v}{\partial z} = 0,\\
&\text{at } x = 0: \quad u = U_o,\ v = V_o,\ w = 0,\\
&\text{at } x = x_i: \quad p = 0.
\end{aligned} \tag{21}$$

The momentum integral method [33] is used to solve the set of Eqs. (16)–(20) along with boundary conditions (21). In order to obtain a solution, the shape of the velocity profiles must be specified. Using streamline coordinates, the velocity components in the streamwise direction, u_s, and in the crossflow direction, u_n, are defined as functions of $\eta = z/\delta(x)$ inside the boundary layers: $\frac{u_s}{q_c} = f(\eta)$ and $\frac{u_n}{q_c} = \varepsilon\, g(\eta)$. Where $\tan^{-1}\varepsilon$ is the angle between the directions of the surface limiting streamline and the streamline of the external flow, at the core region where the fluid velocity is q_c. The crossflow profile is induced because the lower-momentum fluid near the wall responds more rapidly to the pressure gradient than higher-momentum fluid in the core, therefore skewing the velocity vector across the boundary layer. With this coordinate system it is easy to see that the conditions that $f(\eta)$ and $g(\eta)$ must satisfy are: $f(0) = 0$, $g(0) = 0$, $f(1) = 1$, and $g(1) = 0$. Chosen functions are, a typical Kármán-Pohlhausen profile for the streamwise flow and a Mager crossflow profile [33,34],

$$f(\eta) = 2\eta - 2\eta^3 + \eta^4, \qquad g(\eta) = (1-\eta)^2 f(\eta). \tag{22}$$

Rewriting the radial and tangential velocity components in the cylindrical system of coordinates, we get

$$u(x,z) = \begin{cases} u_c(x)f(\eta) + \varepsilon(x)v_c(x)g(\eta), & \text{for } 0 \leqslant \eta \leqslant 1 \\ u_c(x), & \text{for } \eta > 1 \end{cases}, \tag{23}$$

$$v(x,z) = \begin{cases} v_c(x)f(\eta) - \varepsilon(x)u_c(x)g(\eta), & \text{for } 0 \leqslant \eta \leqslant 1 \\ v_c(x), & \text{for } \eta > 1 \end{cases}. \tag{24}$$

When u and v are replaced into the integral equations of motion, along with the chosen profile functions, the following constants are defined: $\alpha_0 = \frac{\mathrm{d}f}{\mathrm{d}\eta}\big|_{\eta=0}$, $\alpha_1 = \int_0^1 f^2(\eta)\mathrm{d}\eta$, $\alpha_2 = \int_0^1 f(\eta)g(\eta)\mathrm{d}\eta$, $\alpha_3 = \int_0^1 g^2(\eta)\mathrm{d}\eta$, $\alpha_4 = \int_0^1 g(\eta)\mathrm{d}\eta$ and $\alpha_5 = \int_0^1 f(\eta)\mathrm{d}\eta$. Replacing these constants, a system of first order ordinary differential equations is obtained for the unknowns δ, u_c, v_c, ε, and p which are all functions only of x. For more information on the resulting equations, readers are referred to Herrmann-Priesnitz et al. [19].

Using the flow model described above, the fluid dynamics has been reduced to an initial value, which is solved using a space marching technique. A problem exists in starting the solution at $x = 0$ because the boundary layer thickness, δ, appears in a denominator in the equations. Therefore, an initial value other than $\delta = 0$ must be specified. Considering a first step of size Δx, an initial value for δ is estimated based on the flow over a flat plate. Hence, the following initial conditions are used at $x = 0$:

$$\delta = 5\sqrt{\frac{5\ \Delta x}{U_o Re}},\ u_c = U_o,\ v_c = V_o,\ \varepsilon = 0,\ p = 0.$$

It is noted that the solutions obtained do not depend critically upon the starting values of δ. In fact, solutions with changes of 50% on the initial values of δ were obtained using different values of Δx. These solutions differed less than 1% by $x = 1 \times 10^{-6}$ and differed less than 0.1% by $x = 0.005$, as shown in Table 1.

In some cases, a very small step size was required for numerical stability near $x = 0$. An adaptive multi-step method was used to reduce the computational time. A 4th order Adams predictor-corrector integration scheme was used, initialized with a 4th order Runge Kutta. Solution was started with $\Delta x = 10^{-8}$ and the local truncation error between the predictor and corrector steps was evaluated to adjust the step size. During each step, the results where checked to see if boundary layers become non entraining, which happens when $u_c = 0$. In that case, the corresponding simplified equations where solved with the same method to calculate δ, v_c ε, and p. Merging of the boundary layers was also monitored during each step.

Table 2
Design parameters for the experimental device of Ruiz and Carey [10].

β	h	r_o	r_i	T_o
9.46°	300 μm	1 cm	0.15 cm	20 °C

3.2. Temperature field

Time marching is used to solve the evolution of the temperature field until steady-state is reached. To achieve this, the transient term, $\frac{\partial \Theta}{\partial t}$, is included in Eq. (15). The resulting partial differential equation is solved by marching in the radial direction from $x = 0$ to x_i in every time step. Chebyshev spectral collocation is used to calculate derivatives in the z direction, a second-order upwind scheme is used to differentiate in x, and an explicit Euler method is used for the time derivative [35–37]. It follows that the complete numerical scheme is:

$$\Theta_j^{n+1} = \Theta_j^n - \Delta t \left[u_j \frac{\left(3\Theta_j^n - 4\Theta_{j-1}^n + \Theta_{j-2}^n\right)}{2\Delta x} + w_j (\mathcal{D}_c.\Theta^n)_j - \frac{1}{RePr} (\mathcal{D}_c^2.\Theta^n)_j \right], \quad (25)$$

where j is the index for the position in the x direction, where the grid spacing is Δx, and n is the index for the time steps which are Δtapart. In Eq. (25), the dot represents matrix product and $\mathcal{D}_c$ is the Chebyshev spectral differentiation matrix.

To ensure numerical stability, the time step size is selected so that the maximum cell Courant number is 1. The cell Courant number, C_u, is calculated as:

$$C_u = \text{Max}\left[\frac{u\Delta t}{\Delta x}, \left(w + \frac{1}{RePr\Delta z}\right)\frac{\Delta t}{\Delta z}\right],$$

where Δz is the cell size in the z direction. The grid used for the temperature field (and to map the velocity field) is uniform in the x direction and Chebyshev in the z direction. Therefore, for N_z points in z, the position of node k is $z_k = \cos(\pi k/(N_z - 1))$, where k goes from 0 to $N_z - 1$. With this type of grid, finer resolution is obtained near the walls, where the gradients are higher. The criteria for convergence to the steady state solution is that the highest value of the time derivative, $\frac{\partial \Theta}{\partial t}$ is less than 10^{-5}. The problem is solved for the boundary conditions shown in Fig. 3.

Grid resolution in the x direction is set to 100 nodes. For the z direction, grid resolution is selected depending on the Reynolds number, 32 nodes are used for $Re < 10$, and 48 nodes for $Re \geq 10$. As Re increases, a finer resolution is required to capture the hydrodynamic boundary layers. The initial condition for the interior nodes is $\Theta = 0$ for low Reynolds numbers. For higher Re, the finer grid demands smaller time steps in order for the scheme to be numerically stable. Therefore, these cases are initialized with the solution obtained for a smaller Reynolds number.

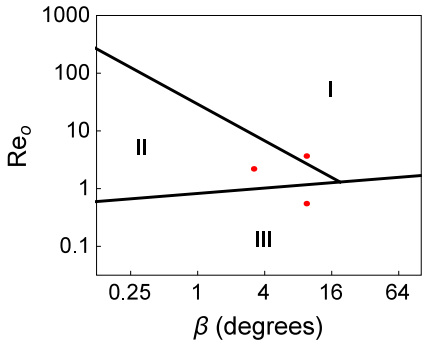

Fig. 6. Classification of boundary layer structure on the β–Re_o space. I: Predominantly entraining. II: Predominantly non entraining. III: Predominantly merged.

4. Validation of numerical results

Ruiz and Carey fabricated a prototype for the swirl flow microchannel heat sink and carried out experimental measurements of the device performance [10]. Distilled water was used as the operating fluid, and volumetric flow rates up to 387 ml/min were used. Important heat sink design parameters used by these authors are shown in Table 2.

Parameters shown in Table 2, corresponding to the experimental device from Ruiz and Carey in Ref. [10], are taken as the base case design for this study. Using the methods presented in the previous section, the total pressure drop, Δp, and the average wall heat flux, q''_w, in the swirl flow microchannel heat sink are calculated. For the numerical calculations, the device is required to maintain wall temperature at $T_w = 80$ °C. Experimental curves for the total pressure drop and the average wall heat flux, with an average wall temperature of 80 °C, are extracted from the results in Ref. [10]. A comparison between the performance curves obtained experimentally and those obtained numerically is presented in Fig. 5.

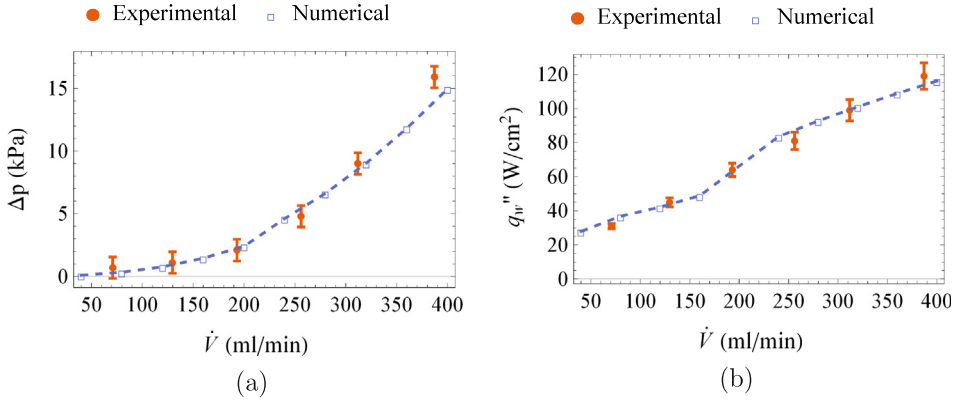

Fig. 5. Performance curves obtained experimentally by Ruiz and Carey in [10] and obtained numerically in the present study: (a) Pressure drop vs flow rate, including entry and exit effects. (b) Average wall heat flux vs flow rate.

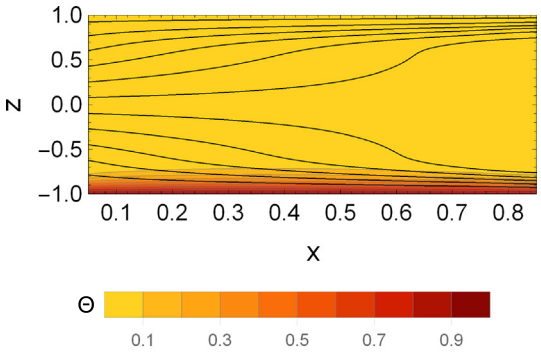

(a) Case 1: $\beta = 9.46^o$, $Re_o = 3.67$, and $Pr = 2.20$.

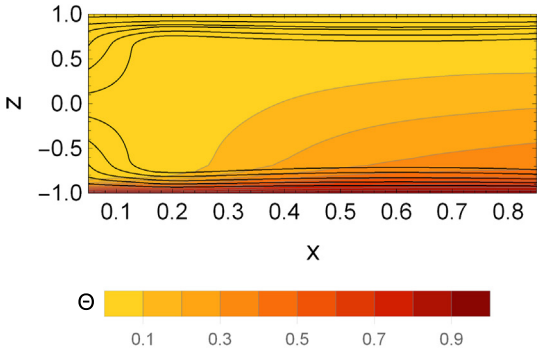

(b) Case 2: $\beta = 3.18^o$, $Re_o = 2.20$, and $Pr = 2.20$.

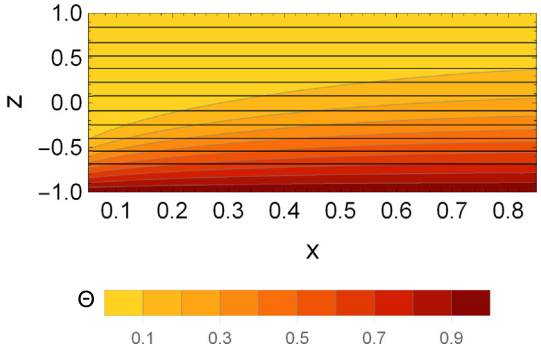

(c) Case 3: $\beta = 9.46^o$, $Re_o = 0.55$, and $Pr = 2.20$.

Fig. 7. Contours of dimensionless temperature, Θ, and streamlines in the x-z plane, where $x = 1 - r^*/r_o$.

For consistency with the experimental device, numerical values for the total pressure drop shown in Fig. 5 also include a standard model for taking into account additional energy losses from entry and exit effects. Specifically, a sudden contraction and sudden expansion are considered at the flow inlet and outlet respectively, as well as a 90° turn in both of these regions [38]. As shown in Fig. 5, numerical results for both, Δp and q''_w, are in good agreement with the experimental results from Ref. [10].

5. Results and discussion

5.1. Structure of hydrodynamic boundary layers

The flow model and integral method are used to calculate the phase-space regarding the structure of the hydrodynamic boundary layers in the flow. A flow rate Reynolds number, Re_o is defined as

$$Re_o = Re\ U_o = \frac{u_o h^2}{4\nu r_o} = \frac{\dot{m}h}{8\pi\nu r_o^2},$$

where $\dot{m}$ is the mass flow rate. The steady-state flow is obtained for 800 combinations of the Re_o and the inlet angle β, ranging from 0.1 to 1000 and from 0.1° to 90°, respectively. As the fluid moves radially inward through the cavity, depending on the non-dimensional parameters, entraining boundary layers can merge, become non entraining or remain as entraining boundary layers. The structure of the boundary layers inside the cavity is assessed by classifying the phenomena as follows:

I. Predominantly entraining: Boundary layers do not merge and remain as entraining boundary layers up to values of x greater than 0.4 ($r^* < 0.6\ r_o$).
II. Predominantly non entraining: Boundary layers do not merge and become non entraining for values of x smaller than 0.4 ($r^* > 0.6\ r_o$).
III. Predominantly merged: Boundary layers merge for values of x smaller than 0.4 ($r^* > 0.6\ r_o$).

Using this classification, the steady-state flow physics of the system is characterized on the β–Re_o space, as shown in Fig. 6.

In Fig. 6 it is shown that boundary layers merge under a certain value of Re_o which increases as β increases. As the flow rate Reynolds number decreases, viscous shear stress becomes stronger than advection and as a consequence boundary layers become thick enough to merge. For $\beta < 19°$ boundary layers are predominantly non-entraining inside a band of Re_o that increases its width as β decreases. The more tangentially the flow enters the cavity, the stronger the crossflow induced by the momentum difference between rotating and near wall flows. This crossflow carries fluid inside the boundary layers radially inward and generates the entrainment of fluid from the core. Predominantly entraining boundary layers are found for large flow rate Reynolds numbers, where the crossflow is not strong enough to carry all the flow rate through the boundary layers.

Table 3
Non-dimensional numbers and predominant boundary layer structures.

Case	β (°)	Re_o	Pr	Boundary layers
1	9.46	3.67	2.20	Entraining (I)
2	3.18	2.20	2.20	Non entraining (II)
3	9.46	0.55	2.20	Merged (III)

5.2. Streamlines and temperature field

Temperature fields are solved to showcase the three different boundary layer structures described in the previous section. Combinations of the flow inlet angle and the Reynolds number used for each case are selected to represent different geometries and operating conditions. A fixed value is used for the Prandtl number, $Pr = 2.20$, as it only depends on the fluid properties. The selected β and Re_o for each case are marked as dots in Fig. 6 and are shown in Table 3, these correspond to values used in the next section to explore the design of the swirl flow microchannel heat sink using water as the operating fluid.

To visualize the velocity field in the $x - z$ plane, streamlines are calculated. Fig. 7 shows the dimensionless temperature distribution, Θ, and streamlines in the $x - z$ plane for the three cases solved. Streamlines provide visualization of the evolution and transitions between the different boundary layer structures. In Fig. 7c

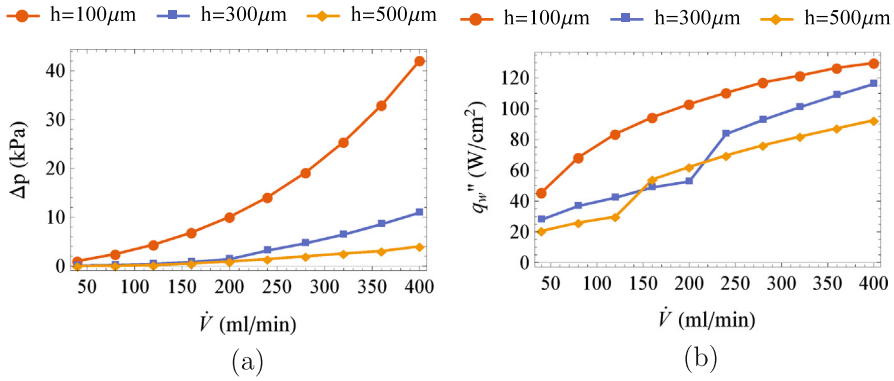

Fig. 8. Performance curves for microchannels of different heights: (a) Pressure drop vs flow rate. (b) Average wall heat flux vs flow rate.

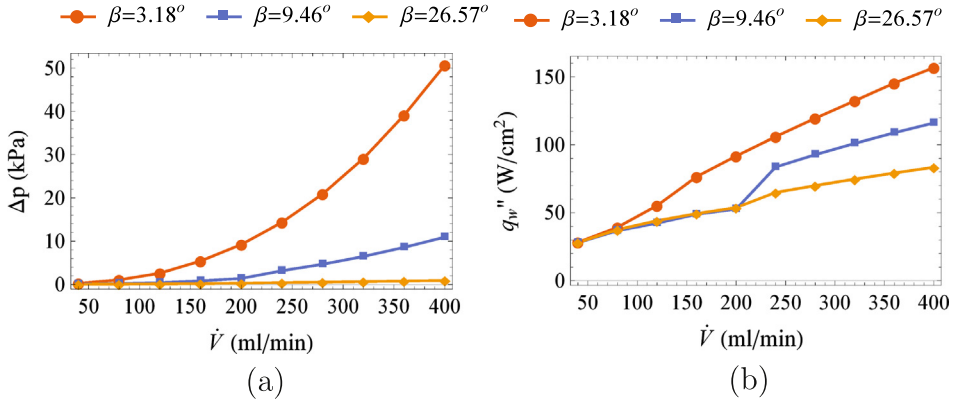

Fig. 9. Performance curves for microchannels with different flow inlet angles: (a) Pressure drop vs flow rate. (b) Average wall heat flux vs flow rate.

streamlines are parallel to each other because boundary layers merge and radial velocity profiles become parabolic. Fig. 7a shows entraining boundary layers, where the movement of fluid towards the walls is induced by the swirl difference between the flow in the core and the flow in the boundary layers. When the swirl is strong enough so that the induced crossflow carries all the flow rate that is passing through the cavity, then non entraining boundary layers develop, as shown in Fig. 7b, and the fluid in the core stays in a pure rotation state. A comparison between Fig. 7b and the flow visualization experiments carried out by Owen et al. [39], identifies the source region observed by these authors as the entraining boundary layers found in this study. Experimental measurements of the velocity field should be carried out in order to make a quantitative comparison with the model.

From the contours of dimensionless temperature, a thermal boundary layer on the lower wall can be recognized. In Fig. 7c the development of the thermal boundary layer resembles that found in the flow between parallel plates. A thinner thermal boundary layer is found in Fig. 7a, because a higher flow rate is concentrated near the walls due to the entrainment. An abrubt increase in the thickness of the thermal boundary layer is observed in Fig. 7b, where the hydrodynamic boundary layers are non entraining. The influence of the higher wall temperature penetrates through the viscous boundary layer and reaches the inviscid core where no velocity gradients are present, therefore the heat transfer mechanism in the core is pure conduction.

Results show that entrainment effects will enhance heat transfer in the swirl flow microchannel heat sink, therefore β and Re_o should be adjusted to manipulate the boundary layer structure. In order to take advantage of this effect, β should be as small as possible, which means that the fluid should be admitted in the microchannel as tangent as possible. For a swirl flow microchannel heat sink of a certain radius, Re_o can be increased by increasing the flow rate or the cavity height. Intuition suggests that the average wall heat flux will increase with the flow rate and decrease with the cavity height, as in conventional microchannel heat sinks. Nonetheless, this may not be the case for the device studied here, as entrainment effects are present when increasing Re_o over a certain value. Heat transfer can also be enhanced by decreasing the Prandtl number, which can be done by changing to a working fluid with a higher thermal conductivity.

5.3. Design exploration

Using the methods presented above, performance of the swirl flow microchannel heat sink can be calculated for a given design. In this section, we consider a base case with the design parameters shown in Table 2, which correspond to the device studied experimentally by Ruiz and Carey in Ref. [10]. Starting from the base case, which uses water as the working fluid, we evaluate the effect of certain design variations on the total pressure drop and average wall heat flux through the device. In particular, the effect of the cavity height, h, the effect of the flow inlet angle, β, and the effect of the Prandtl number, Pr. All heat sink designs are required to maintain wall temperature at $T_w = 80$ °C, use an inlet temperature of $T_o = 20$ °C, and performance is investigated for volume flow rates up to $\dot{V} = \dot{V}_{\max} = 400$ ml/min.

5.3.1. Effect of the cavity height

The effect of the cavity height on the performance of the swirl flow microchannel heat sink is investigated. For this purpose the

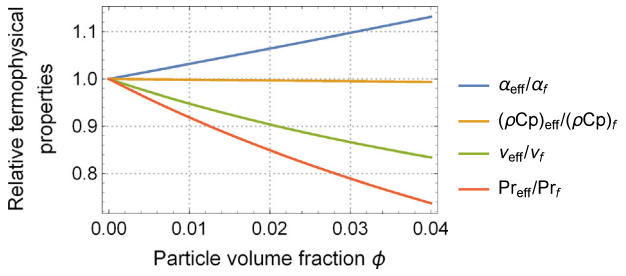

Fig. 10. Suspension relative thermophysical properties: thermal diffusivity, specific heat capacity, kinematic viscosity, and Prandtl number as a function of the particle volume fraction.

total pressure drop, Δp, and the average wall heat flux, q''_w, are calculated for three designs with different cavity heights $h = 100$ μm, 300 μm and 500 μm. Performance curves for flow rates up to $\dot{V}_{\max}$ are shown in Fig. 8.

When the flow rate increases, the total pressure drop through the heat sinks grows at an increasing rate, as shown in Fig. 8a. It is observed that the smaller the height of the cavity, the larger the pressure drop. This effect is due to the reduction in the flow passage area, and becomes more important as the flow rate increases. The average wall heat flux also grows with $\dot{V}$ but at a decreasing rate, as shown in Fig. 8b. For $h = 300$ μm and 500 μm, abrupt increments in q''_w are observed at given flow rates. This happens because, for these cases, hydrodynamic boundary layers merge at low $\dot{V}$ and become non entraining over a critical value of $\dot{V}$. For the design with $h = 500$ μm, streamlines and temperature contours before and after the abrupt increment in q''_w are shown in Fig. 7c and a, which correspond to flow rates of 60 ml/min and 400 ml/min respectively. As shown in Fig. 6, for a given β, this transition occurs at a certain value of Re_o, therefore if height of the cavity increases, then the critical flow rate decreases. Heat transfer is enhanced when boundary layers do not merge because of the flow rate concentration near the walls due to the swirl induced cross-flow and entrainment. For $h = 100$ μm the curve is smooth because hydrodynamic boundary layers always merge for the calculated flow rates.

Reducing the cavity height is desired for high heat flux cooling applications, but only up to a point. The designer should keep in mind Fig. 6 and the structure of the boundary layers, as entrainment enhances heat transfer substantially.

5.3.2. Effect of the flow inlet angle

The effect of flow inlet angle on the performance of the swirl flow microchannel heat sink is investigated. For this purpose the total pressure drop, Δp, and the average wall heat flux, q''_w, are calculated for three designs with different flow inlet angles $\beta = 3.18°$, 9.46° and 26.57°. These angles correspond to $\gamma = 18, 6$ and 3 respectively, where γ is the quotient V_o/U_o. Performance curves for flow rates up to $\dot{V}_{\max}$ are shown in Fig. 9.

As shown in Fig. 9a, the smaller the flow inlet angle, the larger the pressure drop. Due to the increase in the inlet swirl, the pressure gradient must also increase to overcome the centrifugal acceleration, this effect becomes more important as the flow rate increases. The average wall heat flux also grows with a more tangential flow inlet (smaller β), as shown in Fig. 9b. For the base case design, $\beta = 9.46°$, an abrupt increment in q''_w are observed at given flow rates. As discussed in the previous section this happens because, for this case, hydrodynamic boundary layers merge at low $\dot{V}$ and become non entraining over a critical value of $\dot{V}$. As shown in Fig. 6, for a smaller β, this transition occurs for a smaller value of Re_o, therefore if the flow inlet angle decreases, then the critical flow rate also decreases. For $\beta = 3.18°$ boundary layers become non entraining for $\dot{V} > 160$ ml/min, whereas for $\beta = 26.57$ boundary layers never become non entraining. Streamlines and temperature contours for the case with $\beta = 3.18$ at a flow rate of 400 ml/min correspond to those shown in Fig. 7b. It is interesting to point out that the inlet angle has practically no effect over q''_w when boundary layers are merged, as can be observed by comparing the curves for $\beta = 9.46°$ and 26.57° for $\dot{V} \leqslant 200$ ml/min in Fig. 9b. With this in mind, it is clear that boundary layer structure is able to enhance convective heat transfer substantially.

For high heat flux cooling applications the inlet swirl should be increased as much as practically possible. Therefore the design of the fluid admission system will play an important role in the performance of the device. A feeder, plenum chamber, spiral casing, or several injection nozzles should be designed so that fluid is admitted into the cylindrical cavity as tangential as possible.

5.3.3. Effect of the Prandtl number

In order to study the effect of changing the Prandtl number, the working fluid is changed. Convective heat transfer enhancement using a water-Cu nanoparticles suspension is investigated for the swirl flow microchannel heat sink. For this purpose, the effective thermophysical properties of the nanofluid are approximated using several models found in literature [40–44]. For the density a simple volume-weighted average is used:

$$\rho_{\text{eff}} = \rho_{\text{f}}\ (1 - \phi) + \rho_{\text{p}}\ \phi. \tag{26}$$

The same is used for the specific heat capacity:

$$(\rho Cp)_{\text{eff}} = (\rho Cp)_{\text{f}}\ (1 - \phi) + (\rho Cp)_{\text{p}}\ \phi. \tag{27}$$

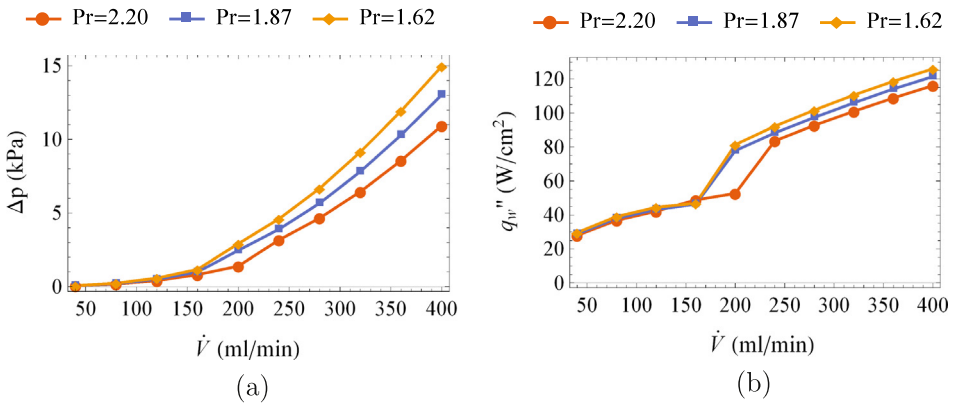

Fig. 11. Performance curves for working fluids with different Prandtl numbers: (a) Pressure drop vs flow rate. (b) Average wall heat flux vs flow rate. (c) Ratio of pumping power to heat rate vs flow rate.

In the year 1952 Brinkman extended Einstein's formula and derived a model for the dynamic viscosity of suspensions with moderate particle concentrations, up to 4 vol% [41]. According to a review by Mishra et al., Ref. [40], the model of Brinkman is widely accepted among researchers:

$$\mu_{\text{eff}} = \frac{\mu_{\text{f}}}{(1-\phi)^{2.5}}. \tag{28}$$

Thermal conductivity is approximated with the expression given by Hamilton and Crosser [42]:

$$\lambda_{\text{eff}} = \lambda_{\text{f}}\left(\frac{\lambda_{\text{p}} + (n-1)\lambda_{\text{f}} - (n-1)\phi(\lambda_{\text{f}} - \lambda_{\text{p}})}{\lambda_{\text{p}} + (n-1)\lambda_{\text{f}} + \phi(\lambda_{\text{f}} - \lambda_{\text{p}})}\right), \tag{29}$$

where n is a shape factor, for a sphere $n = 3$ and for a cylinder $n = 6$. In Eqs. (26)–(29), ϕ is the particle volume fraction, and the subscripts $(\,)_{\text{eff}}$, $(\,)_{\text{f}}$ and $(\,)_{\text{p}}$ denote the thermophysical properties of the suspension, the base fluid and the solid particles respectively.

Performance of the heat sink base case design is investigated for three Prandtl numbers $Pr = 2.20, Pr = 1.87$, and $Pr = 1.62$. These values are obtained using a suspension with water as the base fluid and different concentrations of spherical Cu particles, $\phi = 0$ vol%, 2 vol% and 4 vol% respectively. The properties of copper that were used are $\rho_{\text{p}} = 8933$ kg/m^3, $Cp_{\text{p}} = 385$ J/(kg K), and $\lambda_{\text{p}} = 401$ W/(m K). In order to explain the results, changes in the termophysical properties of the water-Cu nanofluid with the particle volume fraction are calculated using Eqs. (26)–(29) as shown in Fig. 10.

Total pressure drop and average wall heat flux are calculated for the three Prandtl numbers $Pr = 2.20, Pr = 1.87$, and $Pr = 1.62$, which correspond to pure water, a 2 vol% water-Cu nanofluid, and a 4 vol% water-Cu nanofluid, as shown in Fig. 11.

Using the working fluid with lower Prandtl number results in a slight increase of the total pressure drop, as shown in Fig. 11a. This happens because of the lower relative kinematic viscosity associated with the higher particle volume fraction, as shown in Fig. 10, which increases the Reynolds number. With a decrease in the Prandtl number, the average wall heat flux increases for flow rates over 160 ml/min, as shown in Fig. 11b. Because of the decrease in kinematic viscosity, there is an increase in Re_o, therefore the transition to non entraining boundary layers occurs at a lower value of $\dot{V}$. The higher q''_w after the change in boundary layer structure is attributed to this increase in Re_o, as well as the higher thermal diffusivity also associated with the lower Pr. Compared to ν and α, changes in the specific heat capacity are so small that its effect on the total heat flux is negligible.

5.3.4. Heat transfer enhancement

In previous sections, it was found that, compared to the base case design, heat transfer in the device is enhanced when reducing the cavity height, decreasing the flow inlet angle, or lowering the Prandtl number by changing from water to a nanofluid. A comparison of the heat sink performance for these cases, where heat transfer enhancement is observed, is presented. It is also important to compare the average Nusselt number, which is calculated as $Nu = (2h)q''_w/\lambda(T_w - T_m)$, where T_m is the mean temperature in the microchannel. The total pressure drop, average wall heat flux, the ratio of pumping power to heat rate, Q_p/Q_t, and the Nusselt number are shown in Fig. 12.

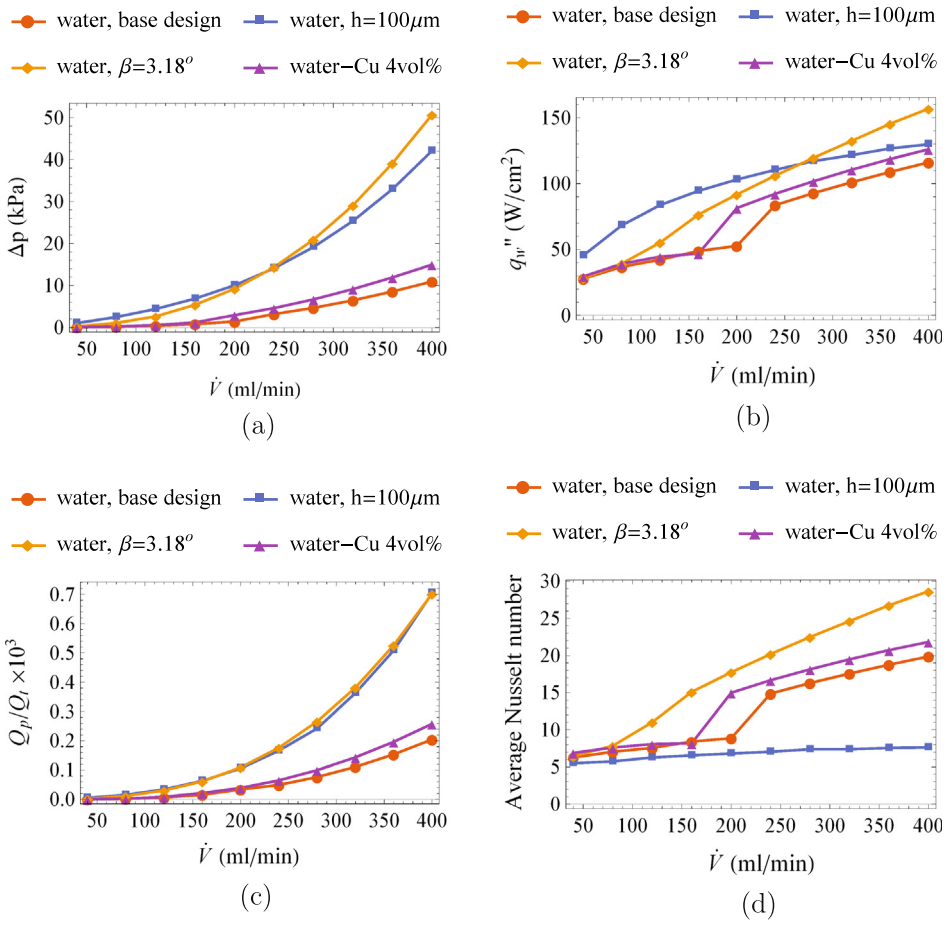

Fig. 12. Performance curves for design variations that present heat transfer enhancement. (a) Pressure drop vs flow rate. (b) Average wall heat flux vs flow rate. (c) Ratio of pumping power to heat rate vs flow rate. (d) Average Nusselt number vs flow rate.

Table 4
Performance of swirl flow microchannel heat sink design variations at $\dot{V} = 400$ ml/min.

Working fluid	h (μm)	β (°)	Δp (kPa)	q''_w (W/cm^2)	Q_p/Q_t ($\times 10^3$)	R_{hs} (K cm^2/W)
Water	300	9.46	10.93	116.11	0.204	0.52
Water-Cu 4 vol%	300	9.46	15.93	128.76	0.269	0.47
Water	100	9.46	42.11	129.66	0.704	0.46
Water	300	3.18	50.71	156.85	0.702	0.38

Heat transfer enhancement reducing the cavity height or decreasing flow inlet angle is greater than that obtained using a working fluid with lower Prandtl number, but at the cost of a greater pressure drop, as shown in Fig. 12a and b. Fig. 12c shows that the ratio of pumping power to heat rate is higher for the variations in h and β, whereas changing to a nanofluid results in a slight increase from the base case. The mechanisms for heat transfer enhancement are identified by comparing the average Nusselt number obtained for the base case to that of the other design modifications in Fig. 12d. It is shown that, Nu is nearly constant with increasing flow rate for merged boundary layers, and it grows with increasing flow rate when entraining effects and secondary flows are present. Therefore, for the reduction in the cavity height, the increase in q''_w is mainly due to an increase in conductive heat transfer. On the other hand, for the change to nanofluid and the decrease in the flow inlet angle, q''_w increases due to convective heat transfer enhancement. In future research, correlations for the average Nusselt number could be established for each type of boundary layer structure.

A parameter commonly used to compare and select heat sinks is the thermal resistance defined as $R_{hs} = (T_w - T_o)/q''_w$. Table 4 shows a summary of the performance characteristics at $\dot{V} = 400$ ml/min of the swirl flow microchannel heat sink designs studied in this section.

Values in Table 4 are compared to data for other devices used for high heat flux applications from the review by Agostini et al. [6]. The average heat flux for the base design of the device studied is about 25% of the highest value reported in the review, nevertheless the ratio of pumping power to heat rate is about 20% of the lowest value listed. The data from Ref. [6] used for comparison is only that of single phase microchannel heat sinks that use water as the operating fluid and are designed to maintain wall temperature below 85 °C, which is a requirement for applications such as thermal management of electronics.

5.4. Physical considerations

Boussinesq approximation is used to account for the thermal buoyancy effects due to gravity. A linear density-temperature relation is used, $\rho = \rho_o[1 - \beta_e(T^* - T_o)]$, where ρ_o is the density at the reference temperature, T_o, and $\beta_e = -1/\rho_o(\partial\rho/\partial T^*)_p$ is the thermal expansion coefficient. Using the scaling presented in Section 2 shows that, compared to the axial presssure gradient, the buoyant gravitational term is of order

$$g\beta_e(T^* - T_o) \sim \mathcal{O}\frac{g\beta_e(T_w - T_o)h/2}{q_o^2}.$$

For the cases studied in this article, even for low flow rates, this term is of order $\sim 10^{-4}$, therefore buoyant effects are neglected.

In the same manner, using the scaling presented in Section 2, the importance of viscous dissipation compared to advection in the thermal energy equation is evaluated. With the boundary layer approximation the viscous dissipation term becomes

$$\frac{\nu}{C_p}\left[\left(\frac{\partial u^*}{\partial z^*}\right)^2 + \left(\frac{\partial v^*}{\partial z^*}\right)^2\right] \sim \mathcal{O}\frac{4\nu q_o r_o}{C_p(T_w - T_o)h^2}.$$

For the cases studied, even for $h = 100$ μm, this term is of order $\sim 10^{-5}$, therefore viscous dissipation is neglected.

Steadiness of the flow is ensured for an incompressible fluid with boundary conditions that do not change in time, as long as the flow is hydrodynamically stable. Rotating flows in cylindrical cavities may become unstable to two different instabilities, designated Types I and II. Type I is usually referred to as inviscid or crossflow instability, and it is related to an inflection point in the velocity profile, similar to the Tollmien-Schlichting instability of the boundary layer on a flat plate, while Type II is called viscous instability and arises from centrifugal or Coriolis forces. Numerous works have been devoted to the investigation of these instabilities [45–50]. Serre et al. studied the stability of Bödewadt layers [46], which are similar to the non entraining boundary layers found in this study. They performed direct numerical simulations and theoretical stability analysis in order to obtain the critical parameters for both type of instabilities: $47.5 \leqslant (Re_\delta)^I_c \leqslant 52.5$ and $18.9 \leqslant (Re_\delta)^{II}_c \leqslant 25.8$, with the Reynolds number defined as $Re_\delta = (v^*_c r^*/\nu)^{1/2}$, where v^*_c is the dimensional tangential velocity at infinity. Similar relations for the critical parameters for entraining and merged boundary layers are not available in the literature. Therefore, future work should investigate the hydrodynamic stability of the flow in order to determine the flow regime for a given combination of nondimensional numbers, for example in the β–Re_o space. The flow model, as presented in this work, is only applicable to laminar flow, nevertheless fully turbulent flow can be studied by adjusting the velocity profiles (1/7th power law could be used) and using an adequate correlation for the skin friction coefficient.

The numerical method developed has a low computational cost, this enables solving a large number of cases and exploring the effect of different variables, providing guidelines for the design of swirl flow microchannel heat sinks. Using the results found here, an improved device should be built and tested experimentally. A plenum chamber, feeder, spiral casing, or several injection nozzles should be used to supply the fluid into the microchannel, with the design emphasizing on reducing β. At the operating flow rate, Re_o should be such that non entraining boundary layers are predominant ($Re_o \sim 1$ for small β), therefore the cavity height should be the smallest that meets this condition.

6. Conclusions

Performance of a swirl flow microchannel heat sink was calculated numerically and the effects of varying the cavity height, h, the flow inlet angle, β, and the working fluid were investigated. Because the numerical method used has a low computational cost, a large number of cases were solved. This allows to study the development of the viscous boundary layers over a wide range of flow rate Reynolds numbers, Re_o, and β. Results show that entraining boundary layers develop for high Re_o, boundary layers merge for low Re_o, and become non-entraining for moderate Re_o and $\beta < 19°$. In order to visualize the evolution and transitions between the different boundary layer structures, streamlines in the $x - z$ plane are plotted along with the temperature distributions.

Total pressure drop and average wall heat flux as a function of flow rate were calculated for different designs. A base case design considers a cavity height of $h = 300$ μm, a flow inlet angle of $\beta = 9.46°$ and water as the working fluid. To investigate the effect of the cavity height, performance curves are calculated for $h = 100$ μm and 500 μm and compared to those of the base design. Results show that pressure drop increases with decreasing h due to the reduction in flow passage area. In addition, abrupt increments are observed in the average heat flux when boundary layers do not merge, because the flow entrainment causes fluid to be drawn towards the walls. It is interesting that unlike what happens in

conventional microchannels, reducing the height may not always result in heat transfer enhancement due to boundary layers merging. When this occurs, the entrainment effect is lost, therefore the total heat flux may decrease.

To investigate the effect of the inlet angle, cases with $\beta = 3.18°$ and 26.57° were compared to the base design. Results show that pressure drop increases when β decreases, which is due to the increase in the inlet swirl and consequentially larger centrifugal acceleration. When Re_o is low enough so that boundary layers merge, the inlet angle has negligible effect over the average wall heat flux. Nevertheless, heat transfer enhancement is observed when β decreases for entraining and non-entraining boundary layers. Therefore, for high heat flux applications, fluid should be admitted into the microchannel as tangential as practically possible.

The effect of reducing *Pr* changing the working fluid was investigated by comparing the performance of the heat sink using water and using a 2 vol% and a 4 vol% water-Cu nanofluid. Effective termophysical properties of the suspension were approximated with models found in the literature. Using the nanofluid results in higher pressure drop and average wall heat flux which is attributed to the lower kinematic viscosity and higher thermal diffusivity. Changing from pure water to a water-Cu nanofluid, the ratio of pumping power to heat rate increases only slightly compared to reducing the microchannel height and inlet angle. The mechanism for heat transfer enhancement when reducing h is conduction, whereas convection is the main mechanism when using a smaller β or changing to a nanofluid.

Device performance was compared to other single phase microchannel heat sinks for high heat cooling applications. Although the swirl flow microchannel heat sink presents about 25% of the heat flux achieved with other devices, the total pressure drop is much lower. This results in a ratio of pumping power to heat rate that is only about 20% of the lowest value reported in the literature reviewed. It can be concluded that the swirl flow microchannel heat sink is suitable for applications were low pumping cost is required. Furthermore, for high heat flux applications, using techniques that enhance heat transfer but also increase the pressure drop would be acceptable.

Future work should consider experimental measurements of the device performance and a theoretical linear stability analysis to determine flow regimes in the β–Re_o space. Instabilities may cause mixing that would further enhance the convective heat transfer, although at a higher pumping cost.

Acknowledgement

B. H-P. thanks CONICYT-Chile for his Ph.D. scholarship CONICYT-PCHA/Doctorado Nacional/2015-21150139.

References

[1] S.G. Kandlikar, W.J. Grande, Evaluation of single phase flow in microchannels for high heat flux chip cooling–thermohydraulic performance enhancement and fabrication technology, Heat Transfer Eng. 25 (8) (2004) 5–16.
[2] M. Datta, H.-W. Choi, Microheat exchanger for cooling high power laser diodes, Appl. Therm. Eng. 90 (2015) 266–273.
[3] A. Royne, C. Dey, D. Mills, Cooling of photovoltaic cells under concentrated illumination: a critical review, Sol. Energy Mater. Sol. Cells 86 (4) (2005) 451–483.
[4] J. Osses-Márquez, W.R. Calderón-Muñoz, Thermal influence on charge carrier transport in solar cells based on GaAs PN junctions, J. Appl. Phys. 116 (15) (2014) 154502.
[5] W.R. Calderón-Muñoz, C. Jara-Bravo, Hydrodynamic modeling of hot-carrier effects in a PN junction solar cell, Acta Mech. (2016) 1–14.
[6] B. Agostini, M. Fabbri, J.E. Park, L. Wojtan, J.R. Thome, B. Michel, State of the art of high heat flux cooling technologies, Heat Transfer Eng. 28 (4) (2007) 258–281.
[7] S.G. Kandlikar, A.V. Bapat, Evaluation of jet impingement, spray and microchannel chip cooling options for high heat flux removal, Heat Transfer Eng. 28 (11) (2007) 911–923.
[8] A.C. Kheirabadi, D. Groulx, Cooling of server electronics: a design review of existing technology, Appl. Therm. Eng. (2016).
[9] M. Ruiz, V.P. Carey, Prediction of Single Phase Heat and Momentum Transport in a Spiraling Radial Inflow Microchannel Heat Sink, No. HT2012-58328, ASME, 2012. Jul.
[10] M. Ruiz, V.P. Carey, Experimental study of single phase heat transfer and pressure loss in a spiraling radial inflow microchannel heat sink, J. Heat Transfer 137 (7) (2015) 071702.
[11] W. Rice, An analytical and experimental investigation of multiple-disk turbines, J. Eng. Power 87 (1) (1965) 29.
[12] K.E. Boyd, W. Rice, Laminar inward flow of an incompressible fluid between rotating disks, with full peripheral admission, J. Appl. Mech. 35 (2) (1968) 229.
[13] B.E. Boyack, W. Rice, Integral method for flow between corotating disks, J. Basic Eng. 93 (3) (1971) 350.
[14] D.N. Wormley, An analytical model for the incompressible flow in short vortex chambers, J. Basic Eng. 91 (2) (1969) 264.
[15] M. Firouzian, J. Owen, J. Pincombe, R. Rogers, Flow and heat transfer in a rotating cavity with a radial inflow of fluid Part 1: The flow structure, Int. J. Heat Fluid Flow 6 (4) (1985) 228.
[16] J. Owen, Air-cooled gas-turbine discs: a review of recent research, Int. J. Heat Fluid Flow 9 (4) (1988) 354.
[17] D. May, J.W. Chew, T.J. Scanlon, Prediction of deswirled radial inflow in rotating cavities with hysteresis, J. Turbomach. 135 (4) (2013) 041025.
[18] B.G. Vinod Kumar, J.W. Chew, N.J. Hills, Rotating flow and heat transfer in cylindrical cavities with radial inflow, J. Eng. Gas Turbines Power 135 (3) (2013) 032502.
[19] B. Herrmann-Priesnitz, W.R. Calderón-Muñoz, E.A. Salas, A. Vargas-Uscategui, M.A. Duarte-Mermoud, D.A. Torres, Hydrodynamic structure of the boundary layers in a rotating cylindrical cavity with radial inflow, Phys. Fluids 28 (3) (2016) 033601.
[20] S. Mochizuki, W.-J. Yang, Heat transfer and friction loss in laminar radial flows through rotating annular disks, J. Heat Transfer 103 (2) (1981) 212.
[21] S. Mochizuki, W.-J. Yang, Local heat-transfer performance and mechanisms in radial flow between parallel disks, J. Thermophys. Heat Transfer 1 (2) (1987) 112–116.
[22] N.V. Suryanarayana, T. Scofield, R.E. Kleiss, Heat transfer to a fluid in radial, outward flow between two coaxial stationary or corotating disks, J. Heat Transfer 105 (3) (1983) 519.
[23] R. Devienne, G. Cognet, Velocity field and heat transfer in a vortex flow exchanger, Wärme Stoffübertragung 25 (3) (1990) 185–191.
[24] Y. Xuan, Q. Li, Heat transfer enhancement of nanofluids, Int. J. Heat Fluid Flow 21 (1) (2000) 58–64.
[25] S.P. Jang, S.U. Choi, Cooling performance of a microchannel heat sink with nanofluids, Appl. Therm. Eng. 26 (17–18) (2006) 2457–2463.
[26] M. Rafati, A. Hamidi, M.S. Niaser, Application of nanofluids in computer cooling systems (heat transfer performance of nanofluids), Appl. Therm. Eng. 45–46 (2012) 9–14.
[27] S. Kakaç, A. Pramuanjaroenkij, Review of convective heat transfer enhancement with nanofluids, Int. J. Heat Mass Transfer 52 (13–14) (2009) 3187–3196.
[28] M. Ghanbarpour, N. Nikkam, R. Khodabandeh, M. Toprak, Improvement of heat transfer characteristics of cylindrical heat pipe by using SiC nanofluids, Appl. Therm. Eng. 90 (2015) 127–135.
[29] J. Wu, J. Zhao, J. Lei, B. Liu, Effectiveness of nanofluid on improving the performance of microchannel heat sink, Appl. Therm. Eng. (2016).
[30] G. Roy, S.J. Palm, C.T. Nguyen, Heat transfer and fluid flow of nanofluids in laminar radial flow cooling systems, J. Therm. Sci. 14 (4) (2005) 362–367.
[31] I. Gherasim, G. Roy, C.T. Nguyen, D. Vo-Ngoc, Experimental investigation of nanofluids in confined laminar radial flows, Int. J. Therm. Sci. 48 (8) (2009) 1486–1493.
[32] I. Gherasim, G. Roy, C.T. Nguyen, D. Vo-Ngoc, Heat transfer enhancement and pumping power in confined radial flows using nanoparticle suspensions (nanofluids), Int. J. Therm. Sci. 50 (3) (2011) 369–377.
[33] H. Schlichting, K. Gersten, Boundary-Layer Theory, Springer, 2000.
[34] A. Mager, 'Generalization of boundary-layer momentum-integral equations to three-dimensional flows including those of rotating system, Tech. Rep. 1067, NACA, 1952.
[35] L.N. Trefethen, Spectral Methods in MATLAB, Cambridge University Press, 2000.
[36] F.S. Alfio Quarteroni, Riccardo Sacco, Numerical Mathematics, Springer, Berlin, Heidelberg, 2010.
[37] D.A.A. Richard, H. Pletcher, John C. Tannehill, Computational Fluid Mechanics and Heat Transfer, Taylor & Francis Inc, 2012.
[38] F.M. White, Fluid Mechanics, McGraw-Hill Education Ltd, 2011.
[39] J.M. Owen, J.R. Pincombe, R.H. Rogers, Sourcesink flow inside a rotating cylindrical cavity, J. Fluid Mech. 155 (1985) 233.
[40] P.C. Mishra, S. Mukherjee, S.K. Nayak, A. Panda, A brief review on viscosity of nanofluids, Int. Nano Lett. 4 (4) (2014) 109–120.
[41] H.C. Brinkman, The viscosity of concentrated suspensions and solutions, J. Chem. Phys. 20 (4) (1952) 571.
[42] R.L. Hamilton, O.K. Crosser, Thermal conductivity of heterogeneous two-component systems, Ind. Eng. Chem. Fund. 1 (3) (1962) 187–191.

[43] S. Murshed, K. Leong, C. Yang, Thermophysical and electrokinetic properties of nanofluids - a critical review, Appl. Therm. Eng. 28 (17–18) (2008) 2109–2125.
[44] G. Puliti, S. Paolucci, M. Sen, Nanofluids and their properties, Appl. Mech. Rev. 64 (3) (2012) 030803.
[45] E. Serre, S. Hugues, E. Crespo del Arco, A. Randriamampianina, P. Bontoux, Axisymmetric and three-dimensional instabilities in an Ekman boundary layer flow, Int. J. Heat Fluid Flow 22 (1) (2001) 82.
[46] E. Serre, E. Tuliszka-Sznitko, P. Bontoux, Coupled numerical and theoretical study of the flow transition between a rotating and a stationary disk, Phys. Fluids 16 (3) (2004) 688.
[47] J.M. Lopez, F. Marques, A.M. Rubio, M. Avila, Crossflow instability of finite Bödewadt flows: transients and spiral waves, Phys. Fluids 21 (11) (2009) 114107.
[48] J. Mizushima, G. Sugihara, T. Miura, Two modes of oscillatory instability in the flow between a pair of corotating disks, Phys. Fluids 21 (1) (2009) 014101.
[49] Y. Do, J.M. Lopez, F. Marques, Optimal harmonic response in a confined Bödewadt boundary layer flow, Phys. Rev. E 82 (3) (2010) 036301.
[50] J.M. Lopez, F. Marques, Rapidly rotating cylinder flow with an oscillating sidewall, Phys. Rev. E 89 (1) (2014) 013013.